Co-generation of hydroxyl and sulfate radicals via homogeneous and heterogeneous bi-catalysis with the EO-PS-EF tri-coupling system for efficient removal of refractory organic pollutants

Co-generation of hydroxyl and sulfate radicals via homogeneous and heterogeneous bi-catalysis with the EO-PS-EF tri-coupling system for efficient removal of refractory organic pollutants

Wanlin Yang[a], Zejun Deng[a,*], Libin Liu[a], Kechao Zhou[a], Sharel P. E[b], Lingcong Meng[c], Li Ma[a,*], Qiuping Wei[a,*]

[a]School of Materials Science and Engineering, State Key Laboratory of Powder Metallurgy, Central South University, Changsha 410083, P.R. China
[b]School of Engineering, University of Edinburgh, Edinburgh, EH9 3DW
[c]School of Chemistry, University of Edinburgh, David Brewster Rd, Edinburgh EH9 3FJ

[*]Corresponding author:
E-mail address: zejun.deng@csu.edu.cn (Dr. Z. Deng); marycsupm@csu.edu.cn (Dr. L. Ma); qiupwei@csu.edu.cn (Dr. Q. Wei).

Abstract: Advanced oxidation processes are commonly considered one of the most effective techniques to degrade refractory organic pollutants, but the limitation of a single process usually makes it insufficient to achieve the desired treatment. This work introduces, for the first time, a highly-efficient coupled advanced oxidation process, namely Electro-Oxidation—Persulfate—Electro-Fenton (EO-PS-EF). Leveraging the EO-PS-EF tri-coupling system, diverse contaminants can be highly efficiently removed with the help of reactive hydroxyl and sulfate radicals generated via homogeneous and heterogeneous bi-catalysis, as certified by radical quenching and electron spin resonance. Concerning degradation of tetracycline (TC), the EO-PS-EF system witnessed a fast pseudo-first-order reaction kinetic constant of 2.54×10^{-3} s^{-1}, ten times that of a single EO system and three-to-four times that of a binary system (EO-PS or EO-EF). In addition, critical parameters (e.g., electrolyte, pH and temperature) are systematically investigated. Surprisingly, after 100 repetitive trials TC removal can still reach 100% within 30 minutes and no apparent morphological changes to electrode materials were observed, demonstrating its long-term stability. Finally, its universality was demonstrated with effective degradation of diverse refractory contaminants (i.e., antibiotics, dyes and pesticides).

Keywords: Electro-Oxidation—Persulfate—Electro-Fenton; Hydroxyl and sulfate radicals; Mechanism; Degradation pathway; Application potential

1 Introduction

Environmentally-related contaminants (e.g., antibiotics, pesticides, industrial chemicals and persistent organic pollutants) are emerging and ubiquitous in the environment, such as the soil, surface water and groundwater, causing devasting threats to the ecological environment and human health. The environmental damage and biological toxicity of these emerging contaminants have developed into a challenging multidisciplinary issue and are yet to be resolved (Johnson et al., 2020; Liu et al., 2021b). Hydroxyl radicals-based advanced oxidation processes (AOPs), also known as deep oxidation processes, are considered one of the most effective techniques to decompose these environmental pollutants owing to their fast reaction rate and capability of completely removing and recycling the treated wastewater (Lu et al., 2022; Zheng et al., 2022). The outstanding feature of AOPs results from the generation of hydroxyl radicals (·OH) with a strong oxidizing ability through homogeneous or heterogeneous catalysis, which is considered the most powerful oxidant to degrade refractory organic pollutants in water.

Among AOPs, the Fenton method is prone to generate ·OH via the homogeneous reaction between Fe^{2+} and H_2O_2, but at the cost of large consumption of H_2O_2 and the production of iron sludge. In addition, this method is only applicable to the limited acidic water pH condition, which significantly narrows the industrial applications toward wastewater treatment. In contrast, no additional H_2O_2 needs supplemented throughout Electro-Fenton (EF) process (Lin et al., 2022). This is because H_2O_2 can be continuously produced by electroreduction of O_2 at the cathode with high overpotentials, followed by a homogeneous reaction with additive Fe^{2+} to generate homogeneous ·OH, and the oxidant (Fe^{3+}) can be reversibly reduced back to Fe^{2+}, as described in Eqs. (1-3) respectively, thus creating a catalytic loop to accelerate the removal of water contaminants (Hu et al., 2021; Liu et al., 2019; Liu et al., 2021a). In addition, heterogeneous ·OH can be generated via Electro-Oxidation (EO) of H_2O on the surface of a "non-active" anode, among which boron-doped diamond (BDD) exhibited the highest ·OH generation efficiency and is considered the ideal anode material for wastewater treatment (see Eq. (4)) (Du et al., 2021). Synergistic effects of combining EO and EF were observed, and this bi-coupling system was capable of greatly enhancing the removal of refractory organic pollutants, such as synthetic wastewater and real wastewater, owing to the dual catalytic treatment via homogeneous ·OH and heterogeneous BDD(·OH) (Nidheesh et al., 2022). However, EO-EF still encountered unsatisfactory limitations such as strict pH control, loss of soluble iron catalyst due to ferric hydroxide precipitation and relatively high energy costs (He and Zhou, 2017).

Sulfate radicals-based AOPs have recently received widespread attention because sulfate radicals ($SO_4^{\cdot-}$) exhibit apparent advantages over ·OH, including relatively higher generation potentials (E^0 = 2.5-3.1 V versus 1.9-2.7 V), stronger selectivity, and longer lifespan (30-40 μs versus 20 ns) respectively. It is noted that $SO_4^{\cdot-}$ can diffuse further to react with contaminants in bulk solution due to its considerably long lifetime (Yang et al., 2021). $SO_4^{\cdot-}$ is generally produced by breaking the peroxygen bond in

peroxymonosulfate or peroxydisulfate. The latest research demonstrated that it could be generated by persulfate (PS) via homogeneous or heterogeneous catalysis with the help of transition metals, electricity, heat, ultrasound, ultraviolet light and quinones (Wang and Wang, 2022). In terms of homogeneous catalysis, Fe^{2+} is considered one of the best candidates for activating PS to generate $SO_4^{\cdot-}$ due to its environmental soundness, high abundance, low cost and high efficiency (see Eq. (5)), as previously reported in the treatment of organic pollutants (Hou et al., 2021; Xiao et al., 2020). As for heterogeneous catalysis, $SO_4^{\cdot-}$ can be efficiently generated via electroreduction of PS (see Eq. (6)) and electrooxidation of SO_4^{2-} (see Eq. (7)), during which PS can be regenerated via electrochemical oxidation of SO_4^{2-} (see Eq. (8)), creating a catalytic loop to greatly reduce the addition of PS (Divyapriya and Nidheesh, 2021). In addition, the introduction of PS in the electrolyte can increase its conductivity and thus the response current (or reduce the cell voltage), which in turn promotes the mass transport of the system and accelerates the degradation efficiency.

Previous studies demonstrated that the combination of EO and PS (EO-PS) allowed the simultaneous generation of heterogeneous ·OH and $SO_4^{\cdot-}$ during electrochemical activation of PS using BDD anode or graphite felt (GF) cathode and demonstrated the synergistic degradation efficiency toward refractory organic pollutants (Bu et al., 2019; Song et al., 2018; Zhi et al., 2020). Arellano et al. (Arellano et al., 2019) introduced the catalyst of iron-based minerals in the EO-PS system for activation of peroxymonosulfate and achieved effective degradation of 1-butyl-1-methylpyrrolidinium chloride. Until now, little research was reported regarding the co-activation of PS by the BDD anode and the GF cathode at the same time, not to mention the synergistic coupling effect in complicated wastewater environments while introducing EF in this system.

Herein, the Electro-Oxidation—Persulfate—Electro-Fenton (EO-PS-EF) triple coupling system was proposed to efficiently degrade refractory organic pollutants via homogeneous and heterogeneous catalytic co-generation of ·OH and $SO_4^{\cdot-}$. Taking TC as the benchmark pollutant, the performance of the single system and the coupled system were systematically compared to assess the coupling effect. Effects of seven key parameters, including the concentration of PS and Fe^{2+}, air flow rate, the species and concentration of inorganic anion, solution pH and temperature, on the degradation performance are considered based on TC removal rate and kinetics. Reactive species in the coupling system are identified by radical quenching and electron spin resonance spectroscopy. The intermediates during TC degradation were analyzed and identified by liquid chromatography-mass spectrometry to determine the possible degradation pathway. In addition, degradation performance (i.e., energy consumption analysis, long-term degradation stability and degradation selectivity) toward additional organic pollutants, including Orange G (OG), Reactive Blue 19 (RB-19), 2,4-Dichlorophenoxyacetic acid (2,4-D) and Atrazine (ATZ), were investigated via the established EO-PS-EF system.

2 Materials and methods

2.1 Chemicals and materials

Tetracycline (TC, >95%), Reactive Blue 19 (RB-19, ≥99.5%), Orange G (OG, ≥96%), Atrazine (ATZ, 97%), 2,4-Dichlorophenoxyacetic acid (2,4-D, 97%), Methanol (MeOH, 99.5%), tert-Butanol (TBA, ≥98%), and 5,5-Dimethyl-1-pyrroline-N-oxide (DMPO, 97%) were purchased from McLean, China. Sodium persulfate (PS, 98%), Ferrous sulfate heptahydrate ($FeSO_4{\cdot}7H_2O$, ≥99%), Sodium sulfate (Na_2SO_4, 99%), Sodium chloride (NaCl, 99.5%), Sodium phosphate (Na_3PO_4, 98%), Sodium carbonate (Na_2CO_3, ≥99.8%), Sodium nitrate ($NaNO_3$, ≥99%), Sodium hydroxide (NaOH, 96%), Sulfuric acid (H_2SO_4, 98%) were purchased from Sinopharm, China. All chemicals were used without further purification. All solutions were prepared with ultrapure water (UPT-I-10T, ACCEXP, China). Graphite felt (GF, 3 mm thickness) was purchased from Jinglong Special Carbon, China. The preparation of flat Ti/BDD used in this work referred to the previous work (Yang et al., 2022a).

2.2 Electrochemical degradation

The electrochemical reactor consisted of a cylindrical electrolytic cell, anode, cathode, DC power supply (RD-2030, Suzhou Wanruida, China), collector-type thermostatic heating magnetic stirrer (DF-101S, Shanghai Lichen Bonsi, China) and air pump (SB-748, Zhongshan Songbao, China) (see Scheme 1). The anode was BDD or 304 stainless steel (SS) electrode, and the cathode was GF or SS electrode. The anode and cathode were placed in parallel with an equal geometric area of 4 cm^2 and an interspace of 1 cm. A uniformly distributed aeration device connected to the air pump was placed right below the cathode.

All degradation experiments were performed with a constant direct current model at the fixed value of 0.2 A and the reactor was under constant stirring with a speed of 300 rpm. Before electrochemical degradation, the electrode system was pre-cleaned with a constant current of 0.2 A for 30 min in 50 mM Na_2SO_4 solution. The volume of simulated wastewater is 0.25 L and the initial concentration of organic pollutants is 0.1 mM. The solution pH was adjusted with the concentrated H_2SO_4 and NaOH, and a water bath maintained the reactor temperature. Prior to the degradation experiment, the solution was saturated with O_2 pumped by the compressed air at a flow rate of 0.25 L min^{-1} for 15 min to ensure the electrosynthesis of H_2O_2. The subsequent O_2 concentration was maintained by air supply at various flow rates. Samples were collected at fixed five-minute intervals for analytical determinations, and the initial sample was used as the control. All experiments were repeated at least three times and the averaged data are shown in the text.

2.3 Analysis methods

TC, ATZ and 2,4-D concentrations were measured by high-performance liquid chromatography (HPLC, Agilent LC1290) with an adjustable wavelength UV detector, equipped with an ACE, UltraCore C18 column (2.1 × 75 mm, 2.5 μm). Before analysis, water samples were filtered using Whatman PTFE membranes (0.22 μm). Detailed analytical parameters were provided in the

supplementary materials (see Table S1). The concentrations of OG and RB-19 were measured by UV-visible spectrophotometer (UV-8000S, METASH, China) based on the absorbance at the maximum absorption wavelength (478 nm and 596 nm, respectively). The physicochemical information of these refractory organic pollutants is presented in Table S2.

TC degradation intermediates were characterized by liquid chromatography-mass spectrometry (LC-MS, Agilent LC1290-QQQ-6470) at the column temperature of 40°C and the autosampler temperature of 25°C. The sample was analyzed by electrospray ionization (ESI) in a positive mode over a mass range of 30-600 amu. The supplementary materials refer to mobile phase ratios, gradient elution parameters, and other LC-MS detection information.

The electron spin resonance (ESR, Bruker A300, Germany) was used to detect transient free radicals in the system. At the specified reaction time intervals, 100 µL of the solution near the anode surface was injected into 50 µL of 100 mM DMPO trap using a capillary tube. The ESR measurements were performed with a power of 6.32 mW, a central field of 3510 G, a sweep width of 100 G, and microwave and modulation frequencies of 9.87 GHz and 100 GHz respectively.

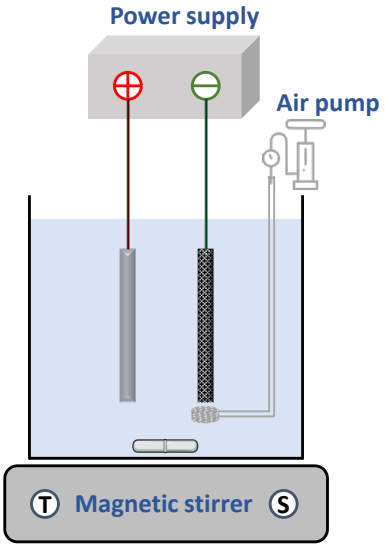

Scheme 1. Schematic illustration of the electrochemical reactor.

3 Results and discussion

3.1 Establishment of the EO-PS-EF tri-coupling system

3.1.1 Synergistic effects of the EO-PS bi-coupling system

Fig. 1 gradually illustrates the establishment of the EO-PS bi-coupling system according to the degradation performance of TC, that is, the removal of TC and corresponding degradation kinetics. Note that statistical analysis of the TC removal by heat map is first introduced to clearly compare and uncover the effects of diverse parameters on the degradation performance. Three key control experiments are first presented in which almost no TC removal after 30 min was observed by GF adsorption or PS alone, or both (see the top panel in Fig. 1), indicating that GF and PS themselves cannot physicochemically remove TC and the unbiased GF cannot activate PS to generate the active radical species, in agreement with the observation from the unbiased BDD electrode (Song et al., 2018).

Previous works indicated that the BDD anode and the GF cathode could activate PS through different reaction mechanisms. Thus, in order to uncover this claim and clarify the contribution of PS activation at the BDD anode and GF cathode toward TC degradation, control experiments were carried out with the stainless steel (SS) electrode, which is difficult to activate PS (Bu et al., 2019). (i) When SS and GF were used as anode and cathode respectively, named as (+)SS|GF(-), partial degradation of TC (11% at 30 min) was observed, which is mainly attributed to the direct oxidation on the SS anode. The addition of 10 mM PS, (+)SS|1X PS|GF(-), increased the TC removal from 11% to 18% at 30 min, and the reaction rate constant (k) increased from 6.52 $\times 10^{-5}$ s^{-1} to 1.09 $\times 10^{-4}$ s^{-1}. The enhanced TC removal was probably attributed to the effective activation of PS at the GF cathode. (ii) When BDD and SS were used as anode and cathode, (+)BDD|SS(-), the TC removal without and with adding 10 mM PS increased to 23% and 33%, accounting for the 12% and 15% increase compared to the counterparts of (+)SS|GF(-), respectively. The improved capability toward TC removal presumably results from the activation of PS on the BDD anode and the GF, while the former exhibited a superior activation performance (10% enhancement ratio after adding 10 mM) than the latter (7% enhancement ratio), indicating the difference in the electro-activation mechanism of PS on the BDD anode and the GF cathode. In addition, the TC removal increased with increasing PS concentrations from 10 mM to 40 mM for both (+)BDD|SS(-) and (+)SS|GF(-) systems, along with enhanced reaction rate constant at high PS concentrations.

At the GF cathode, PS activation to produce $SO_4^{\cdot-}$ is attributed to electrochemical reduction via direct electron transfer (DET). Moreover, superoxide anion ($O_2^{\cdot-}$), which is converted from electrons captured by dissolved O_2 (from the pumping air and oxygen evolution at the anode) at the cathode surface, is a crucial intermediate for PS activation at the GF cathode (Eq. (9) and Eq. (10)) (Bu et al., 2019). A recent study proposed that anodic discharge at the BDD anode could convert adsorbed PS molecules into a special transition state structure PS* (Eq. (11)), which could degrade pollutants as a non-radical oxidation

pathway (Song et al., 2018). At the same time, PS* molecules can promote ·OH production and enhance DET reactions through water hydrolysis at the BDD anode. Notably, $SO_4^{\cdot-}$ and PS can be generated through electrochemical activation of SO_4^{2-}, HSO_4^- or H_2SO_4 owing to the powerful oxidizing capacity of the BDD anode (Divyapriya and Nidheesh, 2021). Meanwhile, the decomposition of $SO_4^{\cdot-}$ and PS will produce a large amount of SO_4^{2-}, which can ensure the recycling of SO_4^{2-}/PS/$SO_4^{\cdot-}$ to a certain extent. The catalytic activation loop of SO_4^{2-}, PS and $SO_4^{\cdot-}$ on the BDD anode endows its better TC degradation performance than the GF cathode activation.

To investigate the activation of PS at both the BDD anode and the GF cathode, 10 mM PS was added to the (+)BDD|GF(-) system, and TC removal, before and after PS addition, was observed to be 37% and 46%, respectively. The addition of PS increased the degradation rate constant from 2.50×10^{-4} s^{-1} to 2.88×10^{-4} s^{-1}, and a synergistic effect of activating PS at the EO-PS bi-coupling system was observed. Later, the effect of PS concentrations (i.e., 10, 20, 30 and 40 mM) on the (+)BDD|GF(-) system was investigated. As the concentration increased from 10 mM to 20 mM, the TC removal increased from 46% to 64% and the reaction rate constant was found to increase from 2.88×10^{-4} s^{-1} to 7.24×10^{-4} s^{-1} respectively, attributed to a significant increase in the activation numbers of PS molecules with increasing concentrations. However, as the concentration continuously increased to 30 mM and 40 mM, the TC removal did not expect to increase but in return, a slight inhibition was observed. These results can be explained by the reorganization of $SO_4^{\cdot-}$ and the consumption of $SO_4^{\cdot-}$ (or ·OH) with excess PS (Eqs. (12-14)), as observed in previous works (Divyapriya and Nidheesh, 2021; Zhang et al., 2021; Zhu et al., 2018). In a nutshell, the PS can greatly promote TC removal at relatively low concentrations (e.g., less than 20 mM), but excess PS (≥ 30 mM) adversely inhibited its removal. Note that the (+)BDD|GF(-) system exhibits faster TC degradation efficiency than the systems of (+)BDD|SS(-) and (+)SS|GF(-) under the identical addition of PS for all concentrations.

The subsequent studies will be carried out under the optimal PS concentration (i.e., 20 mM) on the (+)BDD|GF(-) system, which is named the EO-PS bi-coupling system.

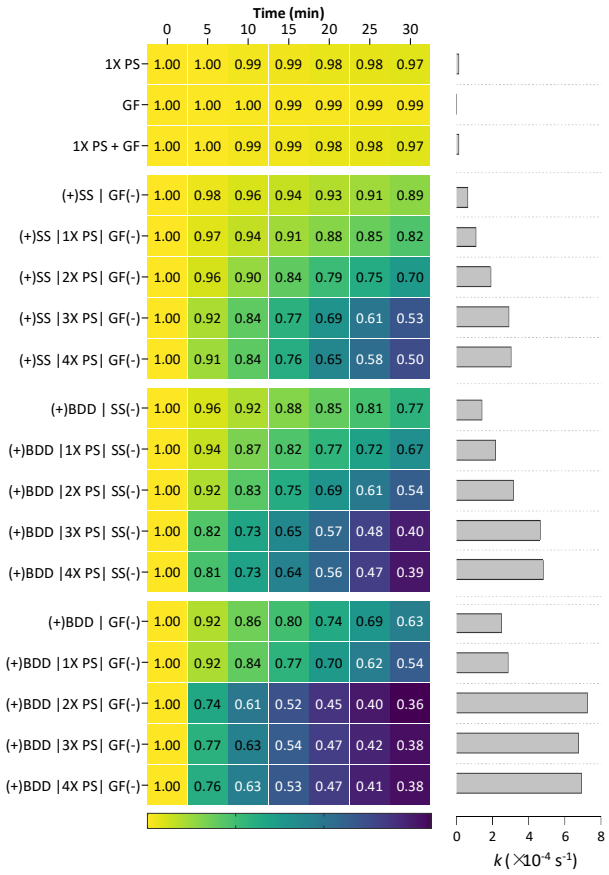

Fig. 1. Establishment of the EO-PS bi-coupling system. (a) Comparative heat map showing the removal rate of TC under various process parameters. 1X, 2X, 3X and 4X PS correspond to 10, 20, 30 and 40 mM PS. The symbol (+) and (-) refers to the anode and cathode respectively. The solution contains 50 mM Na_2SO_4 electrolyte, and pH and temperature are maintained at 7 and 20 °C, respectively. (b) Corresponding pseudo-first-order reaction rate constants.

3.1.2 Synergistic effects of the EO-PS-EF tri-coupling system

In the tri-coupling system, Fe^{2+} and air are considered homogeneous and heterogeneous catalytic co-generation of ·OH and $SO_4^{\cdot-}$. Fig. 2 gradually illustrates the establishment of the EO-PS-EF tri-coupling system. In the EO-PS bi-coupling system, as the Fe^{2+} concentration increased from 0 to 0.1 mM, the TC removal in 5 min increased from 26% to 79%, and the reaction rate constant increased from 7.24×10^{-4} s^{-1} to 3.51×10^{-3} s^{-1}. It was observed that the degradation of TC by the EO-PS-Fe^{2+} system has two-stage reaction kinetic characteristics, with an initial slump and a later decay. In the initial stage, the homogeneous catalytic reaction between Fe^{2+} and PS with a reaction rate constant of up to 4.84×10^{-4} s^{-1} led to the rapid generation of $SO_4^{\cdot-}$,

greatly accelerating the TC removal. After that, most of Fe^{2+} was oxidized to Fe^{3+}, and the reactive oxygen species were mainly supplied via heterogeneous electrochemical reactions with a relatively slow reaction rate, mainly including exclusive BDD anodization ($k = 2.50 \times 10^{-4}$ s^{-1}) and electro-activation of PS ($k = 4.74 \times 10^{-4}$ s^{-1}). In addition, the competing intermediates during the latter period reacted with the reactive species, partially accounting for the decay of TC removal. Thus, TC removal rates dramatically decreased during the heterogeneous reaction period. This phenomenon was also observed from the control experiment with only 0.05 mM Fe^{2+} and 20 mM PS, during which 37% of TC was degraded within 5 min, but only 14% of TC was removed in the following 25 min.

It was noted that Fe(II) and Fe(III) ions have a strong tendency to complex with TC due to the complexation sites of N-type and O-type structures on the A-ring of the TC molecule. The complexation of Fe(II) and TC could accelerate the oxidation of Fe(II), thus promoting the degradation of TC (Zhang et al., 2022). As shown in the control experiment, 0.05 mM Fe^{2+} exclusively achieved 5% TC removal within 30 min owing to the generation of reactive oxygen species (mainly ·OH) while the Fe(II)-TC complex was oxidized to the Fe(III)-TC complex by dissolved oxygen. In addition, the Fe(III)-TC complex could spontaneously transfer to TC oxidation intermediates and Fe(II) (Wang et al., 2016). Thus, the Fe cycle was established between the Fe(II), Fe(III), Fe(II)-TC and Fe(III)-TC, thus promoting TC removal.

The EF system mainly involves the reaction of Fe^{2+} and H_2O_2 to generate ·OH. The formation of H_2O_2 can be achieved by the electrochemical reduction of O_2 at the GF cathode. The EO-EF system was established by adding 0.05 mM Fe^{2+} and the pumping air at a flow rate of 0.25 L min^{-1} to the EO system, which has slightly enhanced degradation performance than the EO-PS system, accounting for 5% higher TC removal. This may be related to the amount of catalysts (Fe^{2+}, aeration and PS), the complexation effect of Fe-TC and the selective oxidation of the dominant active species in different systems. Two parameters of the concentration of Fe^{2+} and the airflow rate were considered to optimize the EO-PS-EF system. Note that as the Fe^{2+} concentration doubled, only 11% of increasing TC removal rate was observed at 5 min and all those concentrations (0.05, 0.75 and 0.1 mM) could achieve 100% of TC removal within a considerable time (less than 30 minutes). Thus, 0.05 mM of Fe^{2+} is chosen for subsequent studies to facilitate comparison and reduce the addition of chemicals. The airflow rate itself did not exhibit the apparent enhancement after addition, only with a 4% improved TC removal rate compared to the bare EO-PS system, and the degradation performance remained unchanged with increasing concentrations (see the 3rd panel in Fig. 2). However, after adding 0.05 mM of Fe^{2+}, Fenton reactions can occur after aeration due to the presence of Fe^{2+}, and the degradation performance of this system greatly increased, constituting a powerful EF system. Undeniably, the introduction of oxygen has a pronounced enhancement effect on the EO-PS-EF system, as observed from the comparison of EO-PS-Fe^{2+} (0.05 mM Fe^{2+}) and EO-PS-EF_1 (0.05 mM Fe^{2+} + 0.25 L min^{-1} Air), with the increment ratio of reaction kinetic constant up to 22% (from 2.08×10^{-3} s^{-1} to 2.54×10^{-3} s^{-1}). However, the effect of continuous enhancement is less significant when the oxygen flow rate further increases from 0.25 L min^{-1} to 1 L min^{-1} (see the bottom panel in Fig. 2). The reason why the degradation of TC did not increase under a high airflow rate could be attributed to the competition of oxygen reduction reaction, hydrogen evolution reaction and PS activation reaction at the GF cathode. In addition, extremely high air flow rates might fill a large amount of air in the reactor, which could hinder electrode/solution contact or even ion transfer. Thus, the airflow rate of 0.25 L min^{-1} was suggested for subsequent studies.

In summary, the EO-PS-EF tri-coupling system was successfully established, which could achieve homogeneous and heterogeneous catalytic co-generation of ·OH and $SO_4^{\cdot-}$ and exhibit powerful degradation performance for TC.

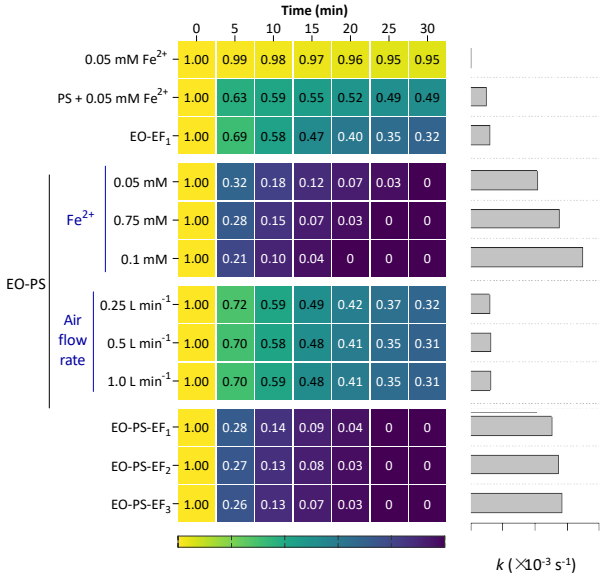

Fig. 2. Establishment of the EO-PS-EF tri-coupling system. (a) Degradation of TC by 0.05 mM Fe^{2+}, 20 mM PS + 0.05 mM Fe^{2+}, EO-EF_1 (0.05 mM Fe^{2+} + 0.25 L min^{-1} Air), EO-PS-Fe^{2+} (0.05, 0.75 and 0.1 mM Fe^{2+}), EO-PS-Air flow rate (0.25, 0.5 and 1 L min^{-1}), EO-PS-EF_1 (0.05 mM Fe^{2+} + 0.25 L min^{-1} Air), EO-PS-EF_2 (0.05 mM Fe^{2+} + 0.5 L min^{-1} Air) and EO-PS-EF_3 (0.05 mM Fe^{2+} + 1 L min^{-1} Air). The solution contains 50 mM Na_2SO_4 electrolyte, and pH is fixed at 7 and temperature at 20 °C. (b) Corresponding pseudo-first-order reaction rate constants.

3.2 Effects of inorganic anion species and concentration

Inorganic anions often act as radical scavengers for the radical-based AOPs and are thus considered. Five common inorganic anion species (NO_3^-, SO_4^{2-}, PO_4^{3-}, CO_3^{2-} and Cl^-) with various concentrations (0, 20, 50 and 100 mM) were comparatively considered, as shown in Fig. 3. NO_3^-, SO_4^{2-}, PO_4^{3-} and CO_3^{2-} adversely inhibited the degradation performance of the EO-PS-EF system, with the inhibition effect of $NO_3^- < SO_4^{2-} < CO_3^{2-} < PO_4^{3-}$. The inhibition phenomenon was improved with increasing ion concentrations, which is more pronounced with SO_4^{2-} and PO_4^{3-}. In contrast, the introduction of Cl^- could promote the removal of TC molecules in the EO-PS-EF system, and the degradation performance was enhanced with increasing concentrations. Among the inhibition ions, NO_3^- has minimal effect on TC removal, and this results from the relatively low reaction rate constant for quenching active radicals (e.g., ·OH and $SO_4^{\cdot-}$). Meanwhile, a high overpotential is required for the oxidation of NO_3^- to $NO_3^{\cdot}$ (see Eqs. (15-17)), as indicated in the previous works (Bu et al., 2018; Huang et al., 2021; Lee et al., 2020). The inhibition effect of SO_4^{2-} was possibly attributed to the limited active adsorption sites on the BDD surface and the competitive adsorption between SO_4^{2-} and PS partially rendered the electro-activation of PS (Cai et al., 2019a; Ding et al., 2020). Under neutral pH, PO_4^{3-} exists in the forms of $H_2PO_4^-$ and HPO_4^{2-} that are not only powerful scavengers of ·OH and $SO_4^{\cdot-}$, but also affect charge consumption (Eqs. (18-23)) (Bu et al., 2018; Wang and Wang, 2020; Xu et al., 2017). The resulting phosphate reactive species (e.g., $HPO_4^{\cdot-}$, $H_2PO_4^{\cdot}$) have too low activities to oxidatively degrade organic pollutants, thus leading to the slump in the degradation performance of the EO-PS-EF system. Similarly, CO_3^{2-} is mainly present in the form of HCO_3^- which is also recognized as a powerful free radical scavenger, and the resulting bicarbonate radical ($HCO_3^{\cdot}$) has low degradation capability (k ranges between 4×10^6 and 1×10^8 M^{-1} s^{-1}) toward organic matters. In addition to scavenging free radicals, HCO_3^- can consume electrons to produce $HCO_3^{\cdot}$ with low oxidative capacity (Eqs. (24-26)) (Lee et al., 2020; Wang and Wang, 2020). The formation of these low reactive oxygen species (ROS) may be responsible for the pronounced inhibition effect of PO_4^{3-} and CO_3^{2-}. Moreover, the competitive adsorption between negatively charged anion species and PS might inhibit PS adsorption and activation.

Interestingly that the presence of Cl^- promoted the degradation of TC in the EO-PS-EF system, and the promotion effect increased with increasing concentrations. This corresponds to the production of highly reactive and strongly selective reactive chlorine species (RCS), which are highly susceptible to addiction, substitution or oxidation reactions with organic compounds with unsaturated bonds and electron-rich groups. It has been demonstrated that RCS reacts faster with certain phenolic compounds (e.g., benzoic acid, bisphenol A) than ·OH and/or $SO_4^{\cdot-}$ (Chen et al., 2022). Cl^- can react with $SO_4^{\cdot-}$ to form chlorine radicals (Cl·) and then dichlorine radical ($Cl_2^{\cdot-}$), and the chlorine products (e.g., Cl· and $Cl_2^{\cdot-}$) can promote the production of ·OH through the reaction, thus accelerating TC removal (see Eq. (27-33)) (Farhat et al., 2017; Oyekunle et al., 2021).

In addition, the influence of the introduction of NO_3^-, PO_4^{3-}, CO_3^{2-} and Cl^- with the same molar concentration on the performance of the system was also studied with 50 mM Na_2SO_4 as the background electrolyte. Its TC removal rate resulted from the mixed effect of the two salts, which was similar to a compromise effect. In general, almost all inorganic anions are capable of consuming electrons and scavenging free radicals with different reaction rates and producing reactive species with varying redox capabilities. The difference in oxidation capacity of these reactive species with respect to the target contaminants determines their impact on water treatment performance.

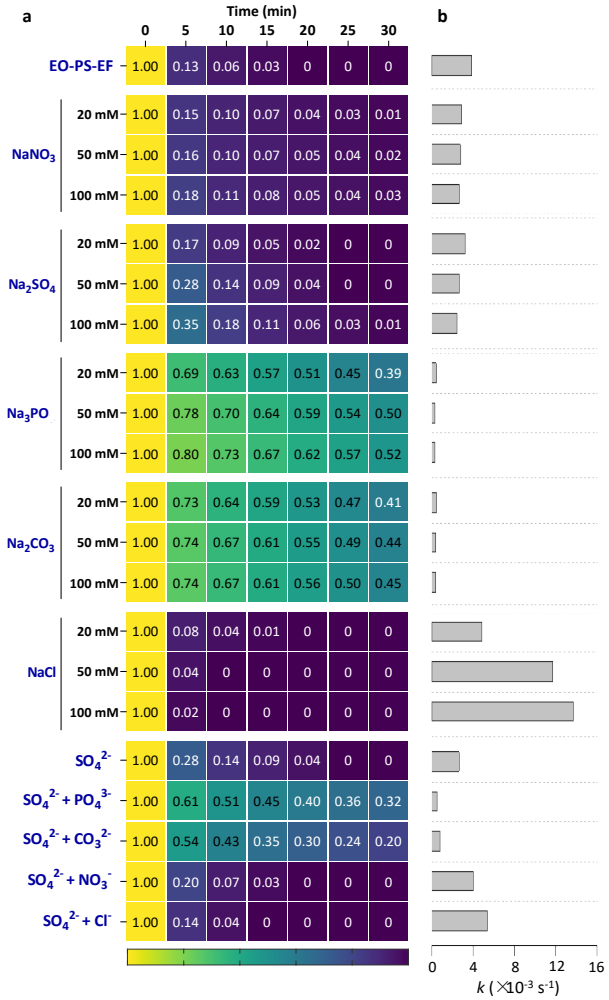

Fig. 3. Effects of inorganic anion species and concentration on the degradation performance of the EO-PS-EF tri-coupling system. (a) Effects of five individual inorganic anions (NO_3^-, SO_4^{2-}, PO_4^{3-}, CO_3^{2-} and Cl^-) at various concentrations (0, 20, 50 and 100 mM) on TC removal. The control experiment (EO-PS-EF_1 without 50 mM Na_2SO_4) was shown on the top panel. (b) Corresponding pseudo-first-order reaction rate constants.

Table 1 Elementary reactions during the EO-PS-EF system.

No.	Reaction equation	E^0 or k	Ref.
1	$O_2 + 2H^+ + 2e^- \rightarrow H_2O_2$	E^0 = 0.67 V vs. RHE	(Hu et al., 2021)
2	$Fe^{2+} + H_2O_2 \rightarrow Fe^{3+} + \cdot OH + OH^-$	k = 40-80 $M^{-1} s^{-1}$	(Liu et al., 2021a)
3	$Fe^{3+} + e^- \rightarrow Fe^{2+}$	E^0 = 0.77 V vs. RHE	(Liu et al., 2019)
4	$BDD + H_2O \rightarrow BDD(\cdot OH) + H^+ + e^-$	E^0 = 1.9-2.7 V vs. RHE	(Du et al., 2021)
5	$Fe^{2+} + S_2O_8^{2-} \rightarrow Fe^{3+} + SO_4^{2-} + SO_4^{\cdot-}$	k = 20-30 $M^{-1} s^{-1}$	(Xiao et al., 2020)
6	$S_2O_8^{2-} + e^- \rightarrow SO_4^{\cdot-} + SO_4^{2-}$	-	(Divyapriya and Nidheesh, 2021)
7	$SO_4^{2-} \rightarrow SO_4^{\cdot-} + e^-$	E^0 = 2.5-3.1 V vs. RHE	(Divyapriya and Nidheesh, 2021)
8	$2SO_4^{2-} \rightarrow S_2O_8^{2-} + 2e^-$	E^0 = 2.01 V vs. RHE	(Divyapriya and Nidheesh, 2021)
9	$O_2 + e^- \rightarrow O_2^{\cdot-}$	-	(Bu et al., 2019)
10	$O_2^{\cdot-} + S_2O_8^{2-} \rightarrow O_2 + SO_4^{\cdot-} + SO_4^{2-}$	-	(Bu et al., 2019)
11	$BDD + PS \rightarrow BDD(PS^*)$	-	(Song et al., 2018)
12	$2SO_4^{\cdot-} \rightarrow S_2O_8^{2-}$	k = 7.6 × 10^8 $M^{-1} s^{-1}$	(Divyapriya and Nidheesh, 2021)
13	$S_2O_8^{2-} + SO_4^{\cdot-} \rightarrow S_2O_8^{\cdot-} + SO_4^{2-}$	k = 6.3 × 10^5 $M^{-1} s^{-1}$	(Zhu et al., 2018)
14	$S_2O_8^{2-} + \cdot OH \rightarrow S_2O_8^{\cdot-} + OH^-$	k = 1.4 × 10^7 $M^{-1} s^{-1}$	(Zhu et al., 2018)
15	$NO_3^- + \cdot OH \rightarrow NO_3^{\cdot} + OH^-$	k < 5.0 × 10^5 $M^{-1} s^{-1}$	(Huang et al., 2021)
16	$NO_3^- + SO_4^{\cdot-} \rightarrow NO_3^{\cdot} + SO_4^{2-}$	k = 5.5 × 10^5 $M^{-1} s^{-1}$	(Huang et al., 2021)
17	$NO_3^- \rightarrow NO_3^{\cdot} + e^-$	E^0 = 2.3-2.5 V vs. RHE	(Bu et al., 2018)
18	$H_2PO_4^- + \cdot OH \rightarrow H_2PO_4^{\cdot} + OH^-$	k = 2.2 × 10^6 $M^{-1} s^{-1}$	(Wang and Wang, 2020)
19	$H_2PO_4^- + SO_4^{\cdot-} \rightarrow H_2PO_4^{\cdot} + SO_4^{2-}$	k < 7 × 10^4 $M^{-1} s^{-1}$	(Wang and Wang, 2020)
20	$HPO_4^{2-} + \cdot OH \rightarrow HPO_4^{\cdot-} + OH^-$	k = 8.0 × 10^5 $M^{-1} s^{-1}$	(Wang and Wang, 2020)
21	$HPO_4^{2-} + SO_4^{\cdot-} \rightarrow HPO_4^{\cdot-} + SO_4^{2-}$	k = 1.2 × 10^6 $M^{-1} s^{-1}$	(Wang and Wang, 2020)
22	$H_2PO_4^- \rightarrow H_2PO_4^{\cdot} + e^-$	-	(Bu et al., 2018)
23	$HPO_4^{2-} \rightarrow HPO_4^{\cdot-} + e^-$	-	(Bu et al., 2018)
24	$HCO_3^- + \cdot OH \rightarrow HCO_3^{\cdot} + OH^-$	k = 8.5 × 10^6 $M^{-1} s^{-1}$	(Lee et al., 2020)
25	$HCO_3^- + SO_4^{\cdot-} \rightarrow HCO_3^{\cdot} + SO_4^{2-}$	k = 9.1 × 10^6 $M^{-1} s^{-1}$	(Wang and Wang, 2020)
26	$HCO_3^- \rightarrow HCO_3^{\cdot} + e^-$	E^0 = 1.7 V vs. RHE	(Wang and Wang, 2020)
27	$Cl^- \rightarrow Cl^{\cdot} + e^-$	E^0 = 2.41 V vs. RHE	(Farhat et al., 2017)
28	$2Cl^- \rightarrow Cl_2^{\cdot-} + e^-$	E^0 = 2.09 V vs. RHE	(Farhat et al., 2017)
29	$Cl^- + SO_4^{\cdot-} \rightarrow Cl^{\cdot} + SO_4^{2-}$	k = 3.2 × 10^8 $M^{-1} s^{-1}$	(Farhat et al., 2017)
30	$Cl^{\cdot} + Cl^- \rightarrow Cl_2^{\cdot-}$	k = 6.5 × 10^9 $M^{-1} s^{-1}$	(Farhat et al., 2017)
31	$Cl^{\cdot} + OH^- \rightarrow HOCl^{\cdot-}$	k = 1.8 × 10^{10} $M^{-1} s^{-1}$	(Farhat et al., 2017)
32	$Cl_2^{\cdot-} + OH^- \rightarrow HOCl^{\cdot-} + Cl^-$	k = 4.5 × 10^7 $M^{-1} s^{-1}$	(Farhat et al., 2017)
33	$HOCl^{\cdot-} \rightarrow \cdot OH + Cl^-$	k = 6.1 × 10^9 $M^{-1} s^{-1}$	(Farhat et al., 2017)
34	$SO_4^{\cdot-} + H_2O \rightarrow SO_4^{2-} + \cdot OH + H^+$	k < 2.0 × 10^3 $M^{-1} s^{-1}$	(Gao et al., 2020)
35	$SO_4^{\cdot-} + OH^- \rightarrow SO_4^{2-} + \cdot OH$	k = 6.5 × 10^7 $M^{-1} s^{-1}$	(Gao et al., 2020)
36	$S_2O_8^{2-} + Heat \rightarrow 2SO_4^{\cdot-}$	-	(Tian et al., 2022)

Note: E^0: Standard reduction potential, k: reaction rate constant

3.3 Effect of pH and temperature

Fig. 4 shows the TC removal of the EO-PS-EF system with respect to pH (top panel) and temperature (bottom panel). The degradation efficiency of TC improves with increasing acidity but decreases with alkalinity. TC removal was observed to be highly efficient in neutral and acidic conditions, and the TC removal reached 96%, 99% and 100% after 20 min at pH of 7, 5 and 3, respectively. However, the TC removal decreased to 69% and 59% at pH of 9 and 11, respectively.

TC molecules have three types of pH-relevant functional groups with different protonation and deprotonation constants (pK_a = 3.3, 7.7 and 9.7), and their forms vary with changing pH, as shown in Fig. S1 (Gao et al., 2022b; Lalliansanga et al., 2022). At pH = 3, most TC molecules were protonated and existed in the cationic form of TCH^+, while at pH = 5 it remained unchanged. At the neutral condition (pH = 7), some TC molecules were transformed into a monovalent anion (TC^-). In contrast, as pH increased to 9, the TC mainly existed in the form of TC^-, while the form of a divalent anion (TC^{2-}) dominated at a pH of 11. When TC species are positively charged, the negative charge on the GF cathode surface facilitates TC adsorption. Also, the lower pH favors the adsorption of PS anions on the cathode, which in turn promotes the generation of $SO_4^{\cdot-}$ (Liu et al., 2018).

The iron species present in the EO-PS-EF tri-coupling system is closely related to solution pH (Dihingia and Tiwari, 2022; Gabriel et al., 2021). On the one hand, iron species are present under alkaline environments in the form of hydroxide complexes such as $FeOH^+$, $Fe(OH)_2^+$, $Fe(OH)_3$ and $Fe(OH)_4^-$, leading to a decrease in the concentration of active Fe^{2+}. The stronger alkaline, the lower the concentration of Fe^{2+}, as shown in Fig. S2. However, Fe^{2+} participated in the generation of $SO_4^{\cdot-}$ from PS and ·OH from H_2O_2. Thus, the degradation performance of the EO-PS-EF tri-coupling system toward TC would be severely inhibited due to the loss of Fe^{2+} in alkaline environments. On the other hand, $SO_4^{\cdot-}$ dominated in acidic conditions while $SO_4^{\cdot-}$ could be converted to ·OH in neutral and alkaline conditions, and ·OH would dominate in relatively concentrated alkaline conditions (see Eq. (34) and Eq. (35)) (Gao et al., 2020). However, the generation potential of ·OH decreased and the oxygen evolution reaction increased under alkaline environments, leading to a decrease in the degradation performance of the EO-PS-EF tri-coupling system. In general, low pH contributes to the removal of TC in EO-PS-EF systems as a result of a comprehensive evaluation of multiple factors.

Later, the critical factor, temperature, was considered under the solution pH of 7. As expected, the degradation performance of the EO-PS-EF system increased with increasing temperatures from 20 °C to 60 °C, and the TC removal within 5 min increased from 72% to 96%, and the reaction rate constant was increased from 2.54 × 10^{-3} s^{-1} to 1.07 × 10^{-2} s^{-1}, respectively. The increase in temperature increased the average kinetic energy of molecules and thus the collision frequency between reactant molecules, increasing the mass transfer and accelerating the activation of PS through the heat to generate more $SO_4^{\cdot-}$ (see Eq. (36)) (Tian et al., 2022). Nevertheless, high temperatures would reduce the solubility of oxygen in the water and adversely

reduce the yield of H_2O_2, unavoidably increasing energy consumption. A balance between removal efficiency and energy consumption should be addressed concerning industrial applications.

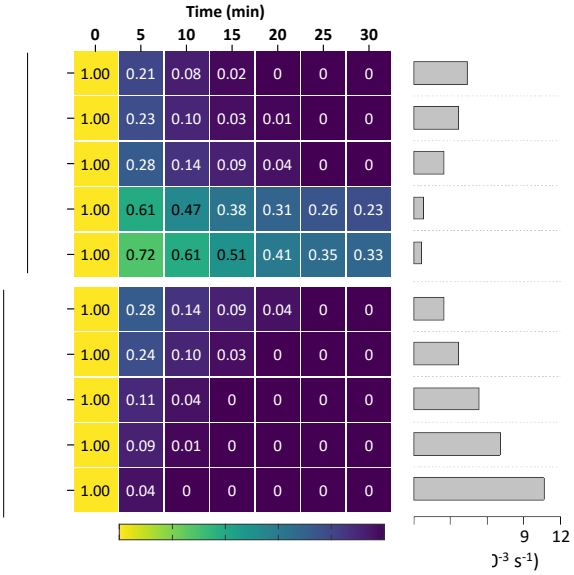

Fig. 4. Effects of pH and temperature on the degradation performance of the EO-PS-EF tri-coupling system. (a) The effect of pH (3, 5, 7, 9 and 11) and temperature (20, 30, 40, 50 and 60 °C) on TC removal in the EO-PS-EF_1 system. The solution pH and temperature were leveled off throughout the degradation period. (b) Corresponding pseudo-first-order reaction rate constants.

3.4 Identification of the major reactive species

3.4.1 Free radicals quenching

MeOH has equivalently high reaction rates to ·OH and $SO_4^{\cdot-}$ ($k_{\cdot OH}$ = 9.7 × 10^8 M^{-1} s^{-1}, $k_{SO_4^{\cdot-}}$ = 1.0 × 10^7 M^{-1} s^{-1}) and was widely used as a scavenger for hydroxyl and sulfate radicals. The reaction rate constant between TBA and ·OH ($k_{\cdot OH}$ = 3.8-7.6 × 10^8 M^{-1} s^{-1}) is three orders of magnitude higher than that between TBA and $SO_4^{\cdot-}$ ($k_{SO_4^{\cdot-}}$ = 4.0-9.1 × 10^5 M^{-1} s^{-1}). Thus, TBA was chosen as a ·OH scavenger (Cai et al., 2019b). The electro-generated active radical species usually exist in the vicinity of the electrode surface, which is different from those homogeneous radical species existed in the bulk solution. Thus, quenching equal concentrations of heterogeneous radical species required higher concentrations of a scavenger than quenching homogeneous radical species, as previously reported (Song et al., 2018). The EO-PS-EF system involves homogeneous catalytic and electrochemical reactions, producing homogeneous and heterogenous radical species. Therefore, the contribution of free radicals evaluated by free radical scavenging studies is of great significance for understanding the reaction mechanism of the EO-PS-EF system. Fig. 5 shows the effects of radical scavenger concentrations (0.1, 1, 2, 4 and 6 M) on the TC degradation performance of the EO-PS-EF system. As the scavenger concentrations increased from 0.1 M to 6 M, the effect of inhibiting TC removal increased. When the concentration of MeOH and TBA was greater than 1 M, the inhibition did not change significantly with further increasing quenchers. Furthermore, we found comparable quenching effects for high-concentration MeOH and TBA, which conflicts with the basic assumption that the added high-concentration quenchers only remove their target active species. This may be related to the confounding effects of high-concentration quenchers that interfere with reactive species production and quench non-target reactive species as reported in the literature (Gao et al., 2022a). For the case of 0.1 M MeOH and 0.1 M TBA, the remaining TC accounts for 44% and 24%, respectively. According to the previous study, it can be distinguished that the respective contributions of ·OH and $SO_4^{\cdot-}$ were 61.6% and 19.3% respectively (Cai et al., 2019b).

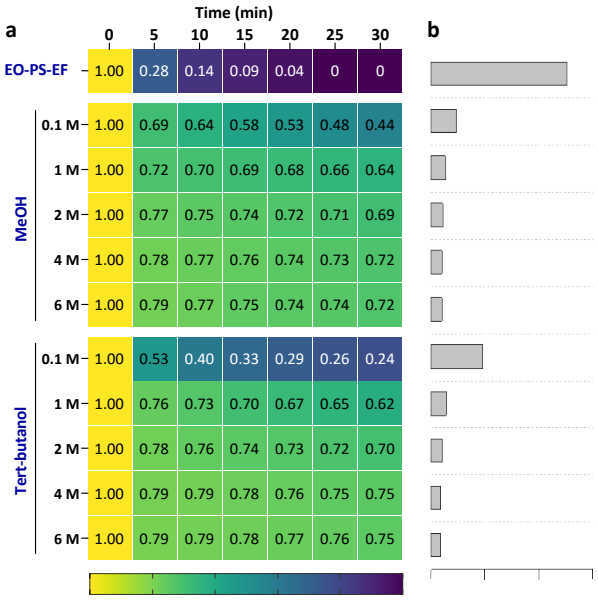

Fig. 5. Free radicals quenching reactions. (a) Effects of MeOH and TBA concentrations on TC removal in EO-PS-EF system. (b) Corresponding pseudo-first-order reaction rate constants.

3.4.2 Electron Spin Resonance

The reactive radicals involved in the EO-PS-EF system were directly determined by the ESR spectroscopy (see Fig. 6). Typical DMPO-OH and DMPO-SO_4 adduct signals were observed based on their hyperfine coupling constants (DMPO-OH: $a_H = a_N = 14.9$ G; DMPO-SO_4: $a_N = 13.2$ G, $a_H = 9.6$ G, $a_H = 1.48$ G, $a_H = 0.78$ G) (Gao et al., 2020). The signal of the DMPO-SO_4 adduct was lower than that of the DMPO-OH adduct in ESR spectrum. This might result from that $SO_4^{\cdot-}$ could be converted into ·OH under neutral and alkaline pH. Besides, the DMPO-SO_4 adduct could also undergo a rapid nucleophilic substitution reaction with H_2O/OH^- forming the DMPO-OH adduct (Gao et al., 2020). According to the relative intensities of the adduct signals, it can be seen that the concentration of free radicals increases with the prolongation of the reaction time, resulting from the accumulation of free radicals. The free radical concentration decreased to a certain extent when the reaction time was further prolonged due to the quenching reaction. In conclusion, ·OH and $SO_4^{\cdot-}$ are the dominant reactive species in the EO-PS-EF system.

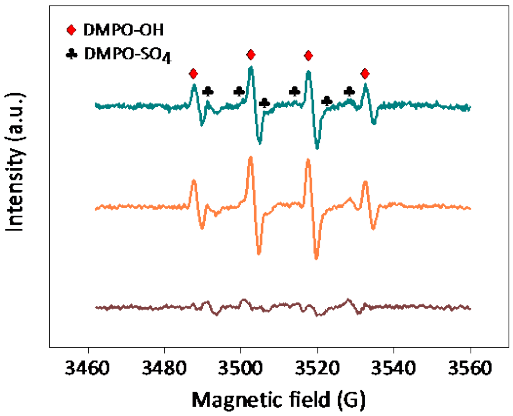

Fig. 6. ESR spectrum recorded at different reaction times of the EO-PS-EF system.

3.5 Degradation mechanism and the pathways

3.5.1 Analysis of the plausible mechanism

Scheme 2 schematically shows the possible degradation mechanism of the EO-PS-EF system. As an ideal anode material, BDD has more substantial oxidation capability and longer service life than other anode materials (e.g., PbO_2, SnO_2, mixed-metal oxides and Ti_4O_7) and can generate heterogeneous ·OH and $SO_4^{\cdot-}$ by anodizing H_2O, PS and SO_4^{2-}. GF is a commercial EF cathode material with low cost, large specific surface area, and stable production yield of H_2O_2, and also allows for cathodic electro-activation of PS. When Fe^{3+} was reduced to Fe^{2+} on the GF surface, the reduced Fe^{2+} would react with PS to generate homogeneous $SO_4^{\cdot-}$. The spontaneous aqueous chemical reactions of Fe^{2+}, H_2O_2 and PS in the bulk solution can generate homogeneous ·OH and $SO_4^{\cdot-}$, respectively. In summary, it is obvious that the homogeneous and heterogeneous catalytic co-generation of ·OH

and $SO_4^{\cdot-}$ is a reasonable mechanism to efficiently remove refractory organic pollutants. Notably, Fe cycling and PS cycling in the EO-PS-EF system might expand its application potential.

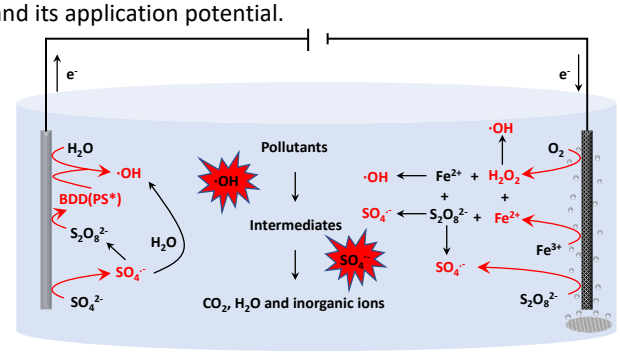

Scheme 2. Schematic illustration of the plausible degradation mechanism of the EO-PS-EF system.

3.5.2 Possible degradation intermediates and pathways

The degradation intermediates of TC were analyzed and identified by LC-MS, which provided a theoretical basis for the degradation pathways and mechanism of TC in the EO-PS-EF system. Various oxidation by-products were detected during TC degradation due to the complexity of TC molecules. 36 intermediates were identified by total ion flow chromatograms and mass spectra with different residence times (Fig. S3 and Table S4). Intermediates were classified into five types such as tetracyclic, tricyclic, bicyclic, monocyclic and short-chain carboxylic acids, according to their structures. Combined with the mechanism of the major reactive species (·OH, $SO_4^{\cdot-}$ and electrons) reacting with organics, a possible degradation pathway of TC in the EO-PS-EF system was proposed (Scheme. 3). Four functional groups can be identified based on the chemical structural formula of TC, including the amide group (-(C=O)-NH_2) and dimethylamine group (-N(CH_3)$_2$) at the C2 position and C4 position of the A ring, the phenolic hydroxyl group (-OH) at the D ring (C10 position) and two conjugated double bond systems of ketone group (R1-(C=O)-R2) and enol group (-C=C-OH) across the ABC ring (Yang et al., 2022b). The electron clouds at these functional group positions were denser and more easily attacked by reactive species to undergo reactions such as electron transfer, double bond addition or hydrogen extraction.

The reaction of TC and reactive species will produce three primary intermediates with m/z = 460, m/z = 416 and m/z = 401. The m/z = 460 primary intermediate was produced by cycloaddition of the double bond (C11a-C12 position) in the TC molecule (Barhoumi et al., 2017; Liang et al., 2018). The m/z = 416 primary intermediate was produced by the demethylation of dimethylamino (-N(CH_3)$_2$) (C4 position). The m/z = 401 primary intermediate was produced by dedimethylamidation (C2 position). The double bond (C2-C3 position) of the m/z = 460 primary intermediate can generate the m/z = 476 intermediate by cycloaddition, further removing the dimethylamino group (C4 position) to produce m/z = 447 intermediate. In addition, the dimethylamino group (-N(CH_3)$_2$) (C4 position) of the m/z = 460 primary intermediate can also undergo an aldehyde conversion reaction to generate the m/z = 474 intermediate, followed by the oxidation of dimethylamino to generate m/z = 432 intermediate. The m/z = 432 intermediate can also be generated from the m/z = 416 primary intermediate by deamination (C4 position) and cycloaddition (C11a-C12 position). The m/z = 432 intermediate can be produced by cycloaddition (double bond at C2-C3 position) and deamidation reaction (C2 position) to produce m/z = 447 and m/z = 407 intermediates. The m/z = 401 primary intermediate then underwent a cycloaddition reaction (C2 position) and removal of the dimethylamino group (C4 position) to generate the m/z = 391 intermediate, which was further subjected to a cycloaddition reaction (C11a-C12 position) can produce m/z = 407 intermediate. Overall, TC molecules formed 9 tetracyclic intermediates in the EO-PS-EF system through cycloaddition, demethylation, deamidation, and deamination reactions. The above tetracyclic intermediates generated 9 tricyclic intermediates (m/z = 451, m/z = 413, m/z = 365, m/z = 349, m/z = 347, m/z = 332, m/z = 317, m/z = 306 and m/z = 274). The ring-opening positions are located at C7-C8, C1-C2, C3-C4 and C1-C12a. Some tricyclic intermediates can be generated by cycloaddition, dehydroxylation, carbonylation or decarboxylation of other tricyclic intermediates. For example, the m/z = 349 intermediate can be produced by oxidation of the m/z = 451, m/z = 413, m/z = 332, m/z = 317 and m/z = 306 intermediates. Further ring opening of these tricyclic intermediates will yield bicyclic (m/z = 250, m/z = 242, m/z = 218) and monocyclic intermediates (m/z = 245, m/z = 230, m/z = 213, m/z = 203, m/z = 201 and m/z = 185). Among them, some intermediates can be produced by the oxidation of other intermediates. For instance, m/z = 230 intermediates can be generated from m/z = 250, m/z = 242, m/z = 203 and m/z = 185 intermediates. Nine short-chain carboxylic acids were identified (m/z = 239, m/z = 223, m/z = 178, m/z = 149, m/z = 118, m/z = 101, m/z = 90, m/z = 71, m/z = 45). m/z = 239 can yield m/z = 223 and m/z = 178 intermediates by sequential oxidation. m/z = 149 can be oxidized to produce m/z = 71. m/z = 118 can be further oxidized to produce m/z = 101. m/z = 90 can be oxidized to produce m/z = 45. Finally, all intermediates might be gradually mineralized into CO_2, H_2O and inorganic ions (Li et al., 2019).

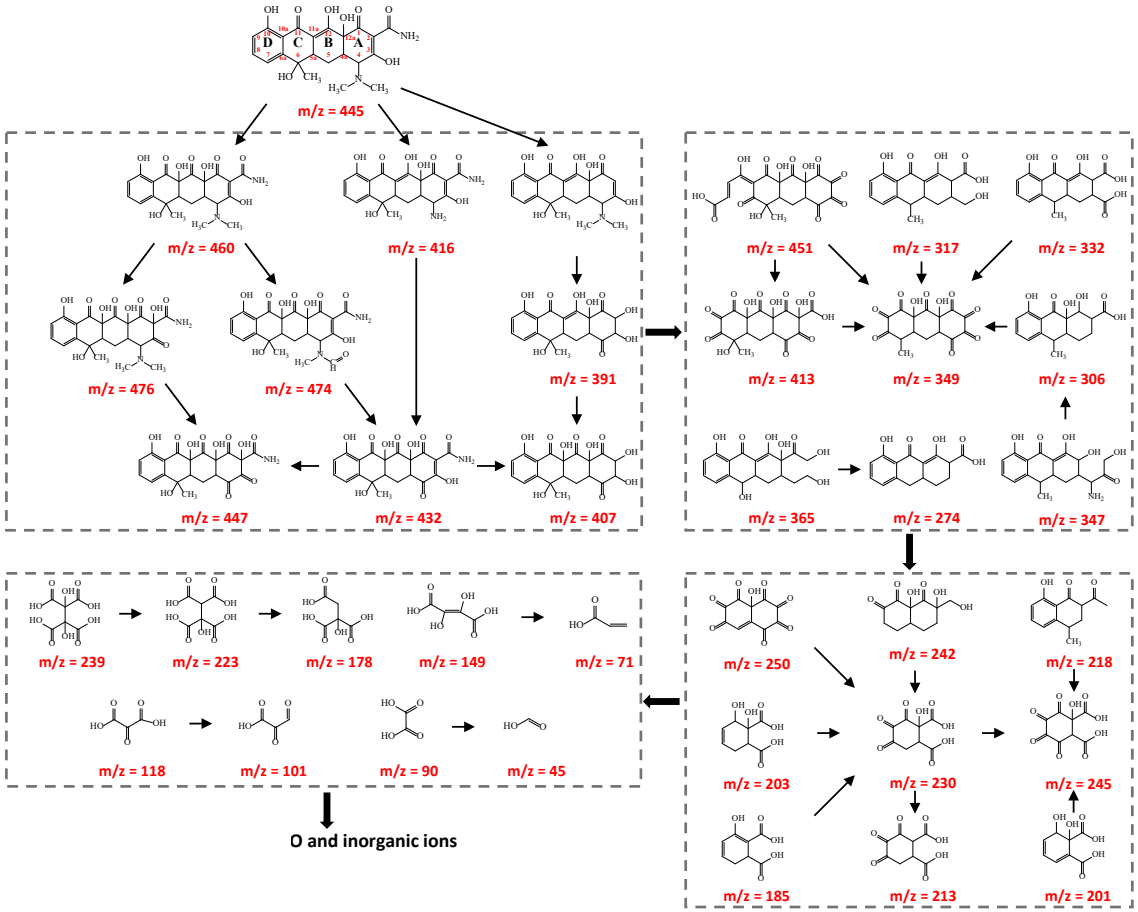

Scheme. 3. The possible degradation intermediates and pathways of TC in the EO-PS-EF system.

3.6 Application potential of EO-PS-EF system

3.6.1 Energy consumption

The electric energy efficiency of these AOPs (i.e., EO, EO-PS, EO-EF and EO-PS-EF) was evaluated based on the energy consumption per cubic meter of contaminant removal (EC, kWh m^{-3}) according to reference (Wei et al., 2020). Under the power consumption of 1.65 kWh m^{-3}, the TC removal of the EO, EO-PS, EO-EF and EO-PS-EF systems was 21%, 60%, 55%, and 100%, respectively (Fig. 7). For the fixed TC removal of 37%, the power consumption of EO, EO-PS, EO-EF and EO-PS-EF systems were calculated to be 3.04, 0.62, 0.75 and 0.17 kWh m^{-3}, respectively. This result indicated that the EO-PS-EF coupling process provided significant advantages over other processes in terms of pollutant removal and energy consumption. Moreover, Table S5 listed a comparison of the EO-PS-EF method with the reported AOPs for the degradation of TC, indicating that the proposed EO-PS-EF method exhibits significantly faster pollutant removal and lower energy consumption than other methods.

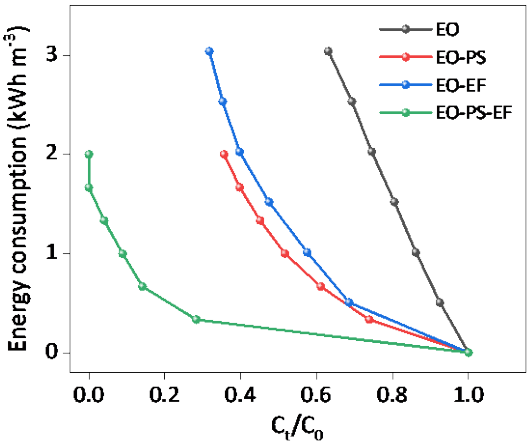

Fig. 7. Comparison of energy consumption related to TC removal rate collected from the EO, EO-PS, EO-EF and EO-PS-EF systems individually.

3.6.2 Long-term stability

The long-term stability of the EO-PS-EF system was considered via repetitive measurements up to 100 times to assess its possible practical applications. Fig. S4 shows repetitive TC removal results taken at the 1st, 25th, 50th, 75th and 100th run. With one-hundred repetitive measurements, the TC degradation performance of the EO-PS-EF tri-coupling system was almost kept unchangeable with only a 5% difference between all runs. In addition, no apparent changes were found in the surface morphologies, phase composition and potential windows of the BDD anode and GF cathode before and after the 100th degradation experiment (Fig. S5 and S6). The degradation tests and experimental observations demonstrated that the EO-PS-EF tri-coupling system had considerably long-term repetitive stability and could run for a quite long lifetime.

3.6.3 Selective degradation of RB-19, OG, ATZ and 2,4-D

Different structural refractory organic pollutants, including Azo dyes (RB-19 and OG) and organochlorine pesticides (ATZ and 2,4-D), were selected as target pollutants to assess the degradation performance of the EO-PS-EF system (see Fig. 8). Other single and bi-coupling systems were also compared including PS, EO, EO-EF and EO-PS. The degradation performance for Azo dyes (RB-19 and OG) are EO-PS-EF > EO-PS > EO-EF > EO > PS, while for organochlorine pesticides (ATZ and 2,4-D) it follows with EO-PS-EF > EO-EF > EO-PS > EO > PS. The comparative results indicate that the bi-coupling system exhibited higher degradation performance than the single system for all Azo dyes and organochlorine pesticides, while the EO-PS-EF significantly improved degradation performance than other single and bi-coupling systems, especially for OG and 2,4-D. The tri-coupling system exhibited exceptional selectivity for 2,4-D that was degraded entirely at around 15 min, with over five times the degradation performance of the other systems. The selectivity preference results from the pollutant structures. The degradation rate is 2,4-D > TC > OG > RB-19 > ATZ for the EO-PS-EF tri-coupling system. This provides an experimental database for the application of the EO-PS-EF system to treat various organic pollutants.

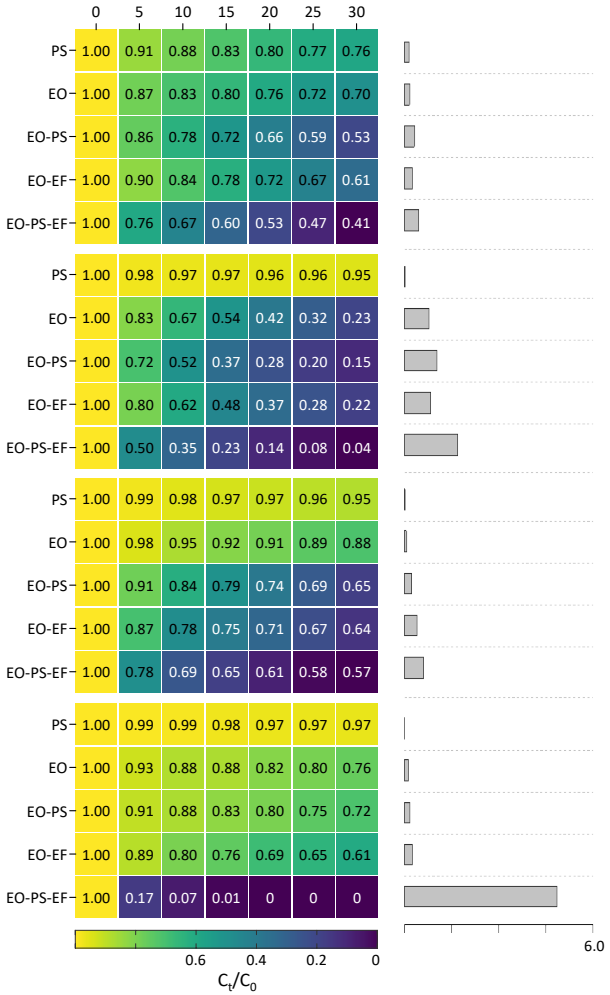

Fig. 8. Comparison of degradation performance of organic pollutants with the PS, EO, EO-PS, EO-EF and EO-PS-EF systems individually, including (a) RB-19, (b) OG, (c) ATZ and (d) 2,4-D. (e) Corresponding pseudo-first-order reaction rate constants.

4 Conclusions

In summary, the EO-PS-EF tri-coupling system based on BDD anode and GF cathode was established for the first time, which efficiently removed pollutants by homogeneous and heterogeneous catalytic co-generation of ·OH and $SO_4^{\cdot-}$. Compared

with PS, EO, EO-PS and EO-EF systems, the EO-PS-EF system can significantly improve pollutant removal efficiency and reduce energy consumption. Adjustment of PS concentration, Fe^{2+} concentration and air flow rate can optimize EO-PS-EF system performance. NO_3^-, SO_4^{2-}, PO_4^{3-} and CO_3^{2-} had different degrees of inhibition on pollutant removal through radicals quenching and electron consumption. However, Cl^- showed a significant promotion effect by generating highly reactive and selective RCS. Besides, low pH and high temperature can facilitate the removal of contaminants. The possible coupling mechanisms and TC degradation pathways of the EO-PS-EF system were revealed based on TC degradation rate constants, radical quenching, ESR and LC-MS data. The high pollution removal efficiency, low energy consumption, long-term cycle stability, and efficient degradation of various pollutants of the EO-PS-EF system demonstrated its potential for practical applications. This study developed an economic, efficient and stable coupling process for removing various emerging pollutants and provided a theoretical basis and experimental foundation for understanding the synergistic mechanism and designing new coupling processes.

Author Contributions

W. Yang: Investigation, Conceptualization, Writing - original draft, Writing - review & editing; Z. Deng: Conceptualization, Validation, Data Curation, Writing - original draft, Writing - review & editing; L. Liu: Resources, Supervision; K. Zhou: Analysis, Suggestion, Resources; S. P. E: Suggestion, Resources; L. Meng: Suggestion, Resources; L. Ma: Resources, Supervision; Q. Wei: Conceptualization, Resources, Funding acquisition, Supervision, Project administration.

Notes

The authors declare no competing financial interest.

Acknowledgments

We gratefully acknowledge the National Key Research and Development Program of China (No.2021YFB3701800), the National Natural Science Foundation of China (No. 52202056, No. 52274370, No. 52071345, No. 51874370), the Province Key Research and Development Program of Guangdong (No. 2020B010185001), the Province High-tech Industry Science and Technology Innovation Leading Plan of Hunan (No. 2022GK4037, No. 2022GK4047) and the Independent and Open projects of the State Key Laboratory of Powder Metallurgy (No. 621022230) for financial support.

References

Arellano, M., Sanroman, M.A. and Pazos, M. 2019. Electro-assisted activation of peroxymonosulfate by iron-based minerals for the degradation of 1-butyl-1-methylpyrrolidinium chloride. Sep. Purif. Technol. 208, 34-41.

Barhoumi, N., Olvera-Vargas, H., Oturan, N., Huguenot, D., Gadri, A., Ammar, S., Brillas, E. and Oturan, M.A. 2017. Kinetics of oxidative degradation/mineralization pathways of the antibiotic tetracycline by the novel heterogeneous electro-Fenton process with solid catalyst chalcopyrite. Appl. Catal. B: Environ. 209, 637-647.

Bu, L.J., Ding, J., Zhu, N.Y., Kong, M.H., Wu, Y.T., Shi, Z., Zhou, S.Q. and Dionysiou, D.D. 2019. Unraveling different mechanisms of persulfate activation by graphite felt anode and cathode to destruct contaminants of emerging concern. Appl. Catal. B: Environ. 253, 140-148.

Bu, L.J., Zhu, S.M. and Zhou, S.Q. 2018. Degradation of atrazine by electrochemically activated persulfate using BDD anode: Role of radicals and influencing factors. Chemosphere 195, 236-244.

Cai, J., Niu, T., Shi, P. and Zhao, G. 2019a. Boron-Doped Diamond for Hydroxyl Radical and Sulfate Radical Anion Electrogeneration, Transformation, and Voltage-Free Sustainable Oxidation. Small 15 (48), 1900153.

Cai, J.J., Zhou, M.H., Pan, Y.W., Du, X.D. and Lu, X.Y. 2019b. Extremely efficient electrochemical degradation of organic pollutants with co-generation of hydroxyl and sulfate radicals on Blue-TiO_2 nanotubes anode. Appl. Catal. B: Environ. 257, 117902.

Chen, C.Y., Wu, Z.H., Hou, S.D., Wang, A.N. and Fang, J.Y. 2022. Transformation of gemfibrozil by the interaction of chloride with sulfate radicals: Radical chemistry, transient intermediates and pathways. Water Res. 209, 117944.

Dihingia, H. and Tiwari, D. 2022. Impact and implications of nanocatalyst in the Fenton-like processes for remediation of aquatic environment contaminated with micro-pollutants: A critical review. J. Water Process Eng. 45, 102500.

Ding, J., Bu, L.J., Zhao, Q.L., Kabutey, F.T., Wei, L.L. and Dionysiou, D.D. 2020. Electrochemical activation of persulfate on BDD and DSA anodes: Electrolyte influence, kinetics and mechanisms in the degradation of bisphenol A. J. Hazard. Mater. 388, 121789.

Divyapriya, G. and Nidheesh, P.V. 2021. Electrochemically generated sulfate radicals by boron doped diamond and its environmental applications. Curr. Opin. Solid St. M. 25 (3), 100921.

Du, X.D., Oturan, M.A., Zhou, M.H., Belkessa, N., Su, P., Cai, J.J., Trellu, P.E. and Mousset, E. 2021. Nanostructured electrodes for electrocatalytic advanced oxidation processes: From materials preparation to mechanisms understanding and wastewater treatment applications. Appl. Catal. B: Environ. 296, 120332.

Farhat, A., Keller, J., Tait, S. and Radjenovic, J. 2017. Assessment of the impact of chloride on the formation of chlorinated by-products in the presence and absence of electrochemically activated sulfate. Chem. Eng. J. 330, 1265-1271.

Gabriel, G.V.D., Pitombo, L.M., Rosa, L.M.T., Navarrete, A.A., Botero, W.G., do Carmo, J.B. and de Oliveira, L.C. 2021. The environmental importance of iron speciation in soils: evaluation of classic methodologies. Environ. Monit. Assess. 193 (2), 63.

Gao, H.Y., Huang, C.H., Mao, L., Shao, B., Shao, J., Yan, Z.Y., Tang, M. and Zhu, B.Z. 2020. First Direct and Unequivocal Electron Spin Resonance Spin-Trapping Evidence for pH-Dependent Production of Hydroxyl Radicals from Sulfate Radicals. Environ. Sci. Technol. 54 (21), 14046-14056.

Gao, L.W., Guo, Y., Zhan, J.H., Yu, G. and Wang, Y.J. 2022a. Assessment of the validity of the quenching method for evaluating the role of reactive species in pollutant abatement during the persulfate-based process. Water Res. 221, 118730.

Gao, P., Ju, C., Tang, Z. and Qin, Y. 2022b. Enhanced adsorption of tetracycline on polypropylene and polyethylene microplastics after anaerobically microbial-mediated aging process. J. Hazard. Mater. Adv. 6, 100075.

He, H.Q. and Zhou, Z. 2017. Electro-Fenton process for water and wastewater treatment. Crit. Rev. Env. Sci. Tec. 47 (21), 2100-2131.

Hou, K.J., Pi, Z.J., Yao, F.B., Wu, B., He, L., Li, X.M., Wang, D.B., Dong, H.R. and Yang, Q. 2021. A critical review on the mechanisms of persulfate activation by iron-based materials: Clarifying some ambiguity and controversies. Chem. Eng. J. 407, 127078.

Hu, J.J., Wang, S., Yu, J.Q., Nie, W.K., Sun, J. and Wang, S.B. 2021. Duet Fe_3C and FeN_x Sites for H_2O_2 Generation and Activation toward Enhanced Electro-Fenton Performance in Wastewater Treatment, Environ. Sci. Technol. 55 (2), 1260-1269.

Huang, W.Q., Xiao, S., Zhong, H., Yan, M. and Yang, X. 2021. Activation of persulfates by carbonaceous materials: A review. Chem. Eng. J. 418, 129297.

Johnson, A.C., Jin, X.W., Nakada, N. and Sumpter, J.P. 2020. Learning from the past and considering the future of chemicals in the environment. Science 367 (6476), 384-387.

Lalliansanga, Tiwari, D., Lee, S.-M. and Kim, D.-J. 2022. Photocatalytic degradation of amoxicillin and tetracycline by template synthesized nano-structured Ce^{3+}@TiO_2 thin film catalyst, Environ. Res. 210, 112914.

Lee, J., von Gunten, U. and Kim, J.H. 2020. Persulfate-Based Advanced Oxidation: Critical Assessment of Opportunities and Roadblocks. Environ. Sci. Technol. 54 (6), 3064-3081.

Li, Z.L., Guo, C.S., Lyu, J.C., Hu, Z. and Ge, M. 2019. Tetracycline degradation by persulfate activated with magnetic Cu/$CuFe_2O_4$ composite: Efficiency, stability, mechanism and degradation pathway. J. Hazard. Mater. 373, 85-96.

Liang, S.T., Lin, H., Yan, X.F. and Huang, Q.G. 2018. Electro-oxidation of tetracycline by a Magneli phase Ti_4O_7 porous anode: Kinetics, products, and toxicity. Chem. Eng. J. 332, 628-636.

Lin, Y.H., Huo, P.F., Li, F.Y., Chen, X.M., Jiang, Y., Zhang, Y.F., Ni, B.J., Zhou, M.H. and Yang, L.Y. 2022. A critical review on cathode modification methods for efficient Electro-Fenton degradation of persistent organic pollutants. Chem. Eng. J. 450, 137948.

Liu, C.F., Huang, C.P., Hu, C.C. and Huang, C.P. 2019. A dual TiO_2/Ti-stainless steel anode for the degradation of orange G in a coupling photoelectrochemical and photo-electro-Fenton system. Sci. Total Environ. 659, 221-229.

Liu, M.Y., Feng, Z.Y., Luan, X.M., Chu, W.H., Zhao, H.Y. and Zhao, G.H. 2021a. Accelerated Fe^{2+} Regeneration in an Effective Electro-Fenton Process by Boosting Internal Electron Transfer to a Nitrogen-Conjugated Fe(III) Complex. Environ. Sci. Technol. 55 (9), 6042-6051.

Liu, Q.F., Li, L., Zhang, X.M., Saini, A., Li, W.L., Hung, H., Hao, C.Y., Li, K., Lee, P., Wentzell, J.J.B., Huo, C.Y., Li, S.M., Harner, T. and Liggio, J. 2021b. Uncovering global-scale risks from commercial chemicals in air. Nature 600 (7889), 456-461.

Liu, Z., Zhao, C., Wang, P., Zheng, H.L., Sun, Y.J. and Dionysiou, D.D. 2018. Removal of carbamazepine in water by electro-activated carbon fiber-peroxydisulfate: Comparison, optimization, recycle, and mechanism study. Chem. Eng. J. 343, 28-36.

Lu, J., Hou, R., Wang, Y., Zhou, L. and Yuan, Y. 2022. Surfactant-sodium dodecyl sulfate enhanced degradation of polystyrene microplastics with an energy-saving electrochemical advanced oxidation process (EAOP) strategy. Water Res. 226, 119277.

Nidheesh, P.V., Ganiyu, S.O., Martinez-Huitle, C.A., Mousset, E., Olvera-Vargas, H., Trellu, C., Zhou, M.H. and Oturan, M.A. 2022. Recent advances in electro-Fenton process and its emerging applications. Crit. Rev. Env. Sci. Tec.

Oyekunle, D.T., Cai, J.Y., Gendy, E.A. and Chen, Z.Q. 2021. Impact of chloride ions on activated persulfates based advanced oxidation process (AOPs): A mini review. Chemosphere 280, 130949.

Song, H.R., Yan, L.X., Jiang, J., Ma, J., Zhang, Z.X., Zhang, J.M., Liu, P.X. and Yang, T. 2018. Electrochemical activation of persulfates at BDD anode: Radical or nonradical oxidation? Water Res. 128, 393-401.

Tian, K., Hu, L.M., Li, L.T., Zheng, Q.Z., Xin, Y.J. and Zhang, G.S. 2022. Recent advances in persulfate-based advanced oxidation processes for organic wastewater treatment. Chinese Chem. Lett. 33 (10), 4461-4477.

Wang, B. and Wang, Y. 2022. A comprehensive review on persulfate activation treatment of wastewater. Sci. Total Environ. 831, 154906.

Wang, H., Yao, H., Sun, P.Z., Li, D.S. and Huang, C.H. 2016. Transformation of Tetracycline Antibiotics and Fe(II) and Fe(III) Species Induced by Their Complexation. Environ. Sci. Technol. 50 (1), 145-153.

Wang, J.L. and Wang, S.Z. 2020. Reactive species in advanced oxidation processes: Formation, identification and reaction mechanism. Chem. Eng. J. 401, 126158.

Wei, Q.P., Liu, G.S., Zhu, C.W., Zhou, B., Mei, R.Q., Ma, L., Zhang, L., Yang, W.L., Ye, W.T., Zhou, K.C. and Yu, Z.M. 2020. Ordered structures with functional units (OSFU) enabled highly robust diamond anode for electrochemical decomposing of organic pollutants. Chem. Eng. J. 397, 125465.

Xiao, S., Cheng, M., Zhong, H., Liu, Z.F., Liu, Y., Yang, X. and Liang, Q.H. 2020. Iron-mediated activation of persulfate and peroxymonosulfate in both homogeneous and heterogeneous ways: A review. Chem. Eng. J. 384, 123265.

Xu, Y., Lin, H., Li, Y.K. and Zhang, H. 2017. The mechanism and efficiency of MnO_2 activated persulfate process coupled with electrolysis. Sci. Total Environ. 609, 644-654.

554 Yang, J.L., Zhu, M.S. and Dionysiou, D.D. 2021. What is the role of light in persulfate-based advanced oxidation for water
555 treatment? Water Res. 189, 116627.
556 Yang, W.L., Deng, Z.J., Wang, Y.J., Ma, L., Zhou, K.C., Liu, L.B. and Wei, Q.P. 2022a. Porous boron-doped diamond for efficient
557 electrocatalytic elimination of azo dye Orange G. Sep. Purif. Technol. 293, 121100.
558 Yang, W.L., Tan, J.L., Chen, Y.H., Li, Z.S., Liu, F.M., Long, H.Y., Wei, Q.P., Liu, L.B., Ma, L., Zhou, K.C. and Yu, Z.M. 2022b.
559 Relationship between substrate type and BDD electrode structure, performance and antibiotic tetracycline mineralization.
560 J. Alloy. Compd. 890, 161760.
561 Zhang, P.Y., Zhang, X.F., Zhao, X.D., Jing, G.H. and Zhou, Z.M. 2022. Activation of peracetic acid with zero-valent iron for
562 tetracycline abatement: The role of Fe(II) complexation with tetracycline. J. Hazard. Mater. 424, 127653.
563 Zhang, W.W., He, Y.C., Li, C., Hu, X.X., Yang, S., You, X.Y. and Liang, W.Y. 2021. Persulfate activation using Co/AC particle
564 electrodes and synergistic effects on humic acid degradation. Appl. Catal. B: Environ. 285, 119848.
565 Zheng, N.C., He, X., Zhou, Q., Wang, R.L., Zhang, X.R., Hu, R.T. and Hu, Z.F. 2022. Generation of reactive chlorine species via
566 molecular oxygen activation on a copper chloride loaded hydrothermal carbonaceous carbon for advanced oxidation
567 process. Appl. Catal. B: Environ. 319, 121918.
568 Zhi, D., Lin, Y.H., Jiang, L., Zhou, Y.Y., Huang, A.Q., Yang, J. and Luo, L. 2020. Remediation of persistent organic pollutants in
569 aqueous systems by electrochemical activation of persulfates: A review. J. Environ. Manage. 260, 110125.
570 Zhu, C.Y., Zhu, F.X., Liu, C., Chen, N., Zhou, D.M., Fang, G.D. and Gao, J. 2018. Reductive Hexachloroethane Degradation by
571 $S_2O_8^{\cdot-}$ with Thermal Activation of Persulfate under Anaerobic Conditions. Environ. Sci. Technol. 52 (15), 8548-8557.